Journal of Materials Chemistry C

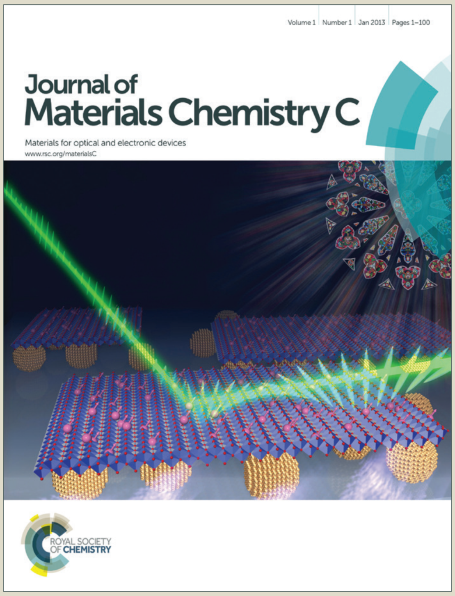

ROYAL SOCIETY OF CHEMISTRY

www.rsc.org/materialsC

Table of contents

Single phase, electrically insulating samples of $Bi_{1-x}La_xFeO_3$ solid solutions have been prepared by mechanosynthesis over the whole compositional range for the first time. Mechanosynthesised samples are free from contamination and the quality of the samples has been proved in terms not only of their structure and microstructure, but also in their physical properties

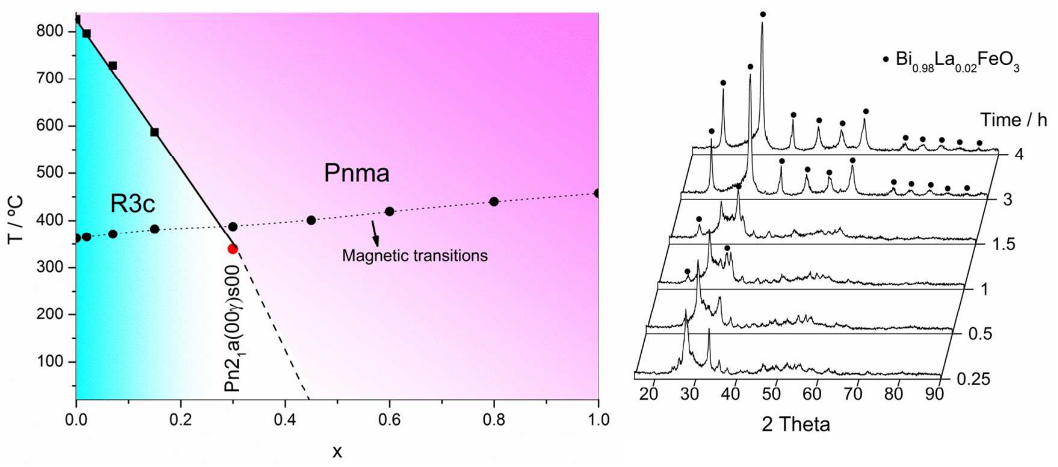

Single phase, electrically insulating, multiferroic La-substituted $BiFeO_3$ prepared by mechanosynthesis†

Antonio Perejón[a,b], Pedro E. Sánchez-Jiménez[a], Luis A. Pérez-Maqueda[a], José M. Criado[a], Julio Romero de Paz[c], Regino Sáez-Puche[d], Nahum Masó[e], Anthony R. West[e]

[a]*Instituto de Ciencia de Materiales de Sevilla (CSIC-Universidad de Sevilla). C. Américo Vespucio 49, Sevilla 41092. Spain*

[b]*Department of Chemistry, Inorganic Chemistry Laboratory, University of Oxford, South Parks Road, Oxford, OX1 3QR, United Kingdom*

[c]*Universidad Complutense de Madrid, CAI Técnicas Físicas, Ciudad Universitaria s/n, Madrid, Spain*

[d]*Departamento Química Inorgánica, Facultad de Ciencias Químicas, Universidad Complutense de Madrid, Ciudad Universitaria, 28040 Madrid, Spain*

[e]*Department of Materials Science and Engineering, University of Sheffield, S1 3JD Sheffield, UK*

Abstract

Single phase, electrically insulating samples of $Bi_{1-x}La_xFeO_3$ solid solutions have been prepared by mechanosynthesis over the whole compositional range for the first time. Lanthanum substitution influenced the kinetics of the mechanochemical reaction and crystallite size of the products. For $0 \leq x \leq 0.15$, an increase in La content produced a significant decrease in the weight-normalized cumulative kinetic energy required to obtain the final product and an increase in the resulting crystallite size. Larger La contents did not affect either reactivity or crystallite size. The effect of x on the structure has been identified. Samples in the ranges $x \leq 0.15$ and $x \geq 0.45$ gave single phase solid solutions with R3c and Pnma space groups, respectively, while for the intermediate range, the non-centrosymetric $Pn2_1a(00\gamma)s00$ super structure was obtained. For $0 \leq x \leq 0.30$, differential scanning calorimetry showed two endothermic effects corresponding to the Néel temperature (T_N, antiferromagnetic-paramagnetic transition) and the Curie temperature (T_C, ferroelectric-paraelectric transition), demonstrating their multiferroic character. Compositions with larger La content only showed T_N. Dilatometric and permittivity measurements confirmed the results obtained by DSC for the ferroelectric-paraelectric transition. The composition dependence of T_N and T_C showed that, at low x, $T_N < T_C$, but a cross-over, or isoferroic transition occurred at $x \sim 0.28$, when $T_N = T_C = 386$ºC. Ceramics with $0 \leq x \leq 0.15$ were highly insulating at room temperature with resistivity, extrapolated from the Arrhenius plots, of $\sim 7 \times 10^{16} - 8 \times 10^{14}$ Ωcm and activation energy ~1.14–1.20 eV. Magnetization of the samples improved with La substitution.

Keywords: $BiFeO_3$, $Bi_{1-x}La_xFeO_3$ solid solutions, mechanosynthesis, impedance spectroscopy, structure identification.

Introduction

Single-phase multiferroic materials are those which present at least two of the so-called "ferroic" properties: ferroelectricity, ferromagnetism and ferroelasticity.[1] Recently, both ferrotoroidic and antiferroic orders are also considered as ferroic properties.[2] In magnetoelectric materials, an electric field induces a magnetization or, alternatively, a magnetic field induces a polarization in the material.[3] The interest in these materials arises from their potential applications in multistate memory devices as FeRAMs and MRAMs for storing binary data, or as magnetoelectric sensors. [4]

$BiFeO_3$ is considered the most promising multiferroic for potential applications because it presents multiferroic properties at room temperature. It has a rhombohedrally-distorted perovskite structure at room temperature with space group R3c, is G-type antiferromagnetic until its $T_{N,}$ 360ºC, and ferroelectric up to $T_{C,}$ 830ºC.[5-7] The main problem in $BiFeO_3$ preparation is the formation of undesired impurity phases, mainly $Bi_{25}FeO_{39}$ and $Bi_2Fe_4O_9$, that lead to deterioration of the electrical and magnetic properties.[8] $BiFeO_3$ presents small spontaneous polarization at room temperature due to a high leakage current and dielectric loss which are attributed to the synthesis methods used and which complicate the study of electrical properties in the low frequency range. The low polarization values are attributed to the presence of secondary phases and to the low resistivity of the ceramics, while leakage current is associated with the presence of Fe^{2+} ions, oxygen vacancies and bismuth evaporation during sintering.[9] The G-type antiferromagnetic ordering in $BiFeO_3$ is superimposed with a space modulated spiral structure, which macroscopically cancels the magnetization.[10] However, the magnetic properties depend greatly on the synthesis procedures and the presence of impurity phases could be responsible for the magnetic properties observed at low temperatures.[11]

The addition of substituents in $BiFeO_3$, taking the positions of either Bi and Fe, has been widely studied and it is possible to find in the literature many papers concerning modifications in $BiFeO_3$ stoichiometry.[12] Apart from solid solutions, mixtures of $BiFeO_3$ with other compounds with perovskite structure have also been considered with the objective of increasing the dielectric constant, reducing the leakage current and improving the ferroelectric polarization.

Rare earth elements, transition metals and alkaline earth metals have all been employed to enhance the dielectric and magnetic properties of $BiFeO_3$, breaking the long-range, spin cycloid superstructure of the antiferromagnetically ordered sublattice responsible for cancelation of the magnetization in distorted perovskites.[13] Special attention has been given to the system $Bi_{(1-x)}R_xFeO_3$, where R is a rare earth element. Partial substitution of Bi^{3+} ions by lanthanides avoids the formation of undesired phases during synthesis and improves the ferroelectric properties and magnetization.[14-34] The most studied system is $Bi_{(1-x)}La_xFeO_3$, also described as (1-x)$BiFeO_3$-x$LaFeO_3$. The first studies demonstrated that the long-range, spin cycloid superstructure disappears in single crystals with 20% La substitution. In bulk materials, La substitution improves the ferromagnetic moment and significantly reduces the leakage current.[35] However, the number of phase transitions and their nature as a function of La content have not yet been clearly determined. Thus, the formation of 3, 5 or even 6 different phases as x increases have been reported.[12, 13, 36-40] Moreover, there is disagreement over the La content that induces phase transitions and the structure that the system adopts once these limits are exceeded. Thus, the value of x required for the rhombohedral (R3c) to orthorhombic transition has been reported in the range from 0.1 to 0.3.[13, 37, 41] It has also been proposed that the R3c and other phases may coexist at the composition limits of each phase.[42] Other authors relate both the phases produced and their stability to Goldschmidt's tolerance factor (t),[43] although in the case of La substitution, the tolerance factor varies little since the ionic radii of both atoms are very similar if an octahedral coordination is assumed (the Bi ionic radius in coordination 12 hasn't been reported), i.e. 1.16 Å for La^{3+} and 1.17 for Bi^{3+}.[44] However, the lone pair orbital of Bi^{3+} ($6s^2$) is stereochemically active and responsible for the ferroelectric distortion. Thus, distortions that still occur on substitution of Bi^{3+} with La^{3+} are more likely to be caused by the diminishing lone-pair activity of Bi.[5]

Electrical properties of lanthanum-substituted $BiFeO_3$ ceramics have been studied mainly at fixed frequencies; a broad dispersion in permittivity as a function of temperature is probably due to variations in sample preparation method. An increase with temperature of permittivity and dielectric loss that is generally observed is related with the antiferromagnetic Néel temperature; a decrease in permittivity and loss as frequency increases, is attributed to a conventional dielectric relaxation process.[9, 45] The permittivity also increases with x, possibly caused by the distortions and structural changes.[46, 47] Surprisingly, the temperature dependence of conductivity is not usually reported in the literature to explain the electrical properties, although Pandit et al. have studied the conduction mechanism in samples prepared by conventional solid state reaction.[48]

Different methods have been proposed for synthesis of the (1-x)$BiFeO_3$-x$LaFeO_3$ system. The most common is conventional solid state reaction, applying different thermal treatments to stoichiometric amounts of the starting oxides; some authors add a small excess of Bi_2O_3 to compensate possible losses by evaporation during synthesis.[9, 13, 37, 42] Other methods include the use of polymeric precursors starting from metal nitrates,[12, 39] and hydrothermal synthesis.[46, 49] Although addition of La seems to facilitate synthesis of substituted $BiFeO_3$, the preparation of phase-pure samples is still an issue in many reports.

The use of mechanosynthesis[50, 51] for obtaining this kind of material is much less studied; there are a few papers, mostly for pure $BiFeO_3$ [52-56] or with certain substituents and in mixtures,[57, 58] but there are no reports of the preparation of La-substituted $BiFeO_3$ by this method. We previously reported[59, 60] that $BiFeO_3$ prepared by mechanosynthesis is phase-pure, highly insulating and not susceptible to reduction, in contrast to other results which report lossy or semiconductive $BiFeO_3$. It is therefore of interest to use this methodology to investigate the synthesis and properties of substituted $BiFeO_3$ materials.

The objective of this work is the preparation by mechanosynthesis of $Bi_{1-x}La_xFeO_3$ solid solutions covering the whole compositional range $0<x<1$. Products are characterized by XRD, Raman spectroscopy, SEM, DSC, dilatometry, impedance spectroscopy and magnetic susceptibility measurements.

Experimental section

Sample preparation

Samples were prepared from commercially available oxides: Bi_2O_3 (Sigma-Aldrich 223891-500G, 10 µm, 99.9% purity), Fe_2O_3 (Sigma-Aldrich 310050-500G, <5 µm, ≥99% purity) and La_2O_3 (Sigma-Aldrich L4000-100G, ≥99% purity). Starting oxides did not require drying, as determined by thermogravimetry. Stoichiometric amounts were mechanically ground under 7 bars of O_2 pressure using a planetary mill Pulverisette 7 (Fritsch, Idar-Oberstein, Germany), modified by incorporating a rotary valve that allowed connection of the jar (sealed with a Viton o-ring and equipped with a male taper straight adaptor) to the gas cylinder during milling. Thus, the pressure inside the jar was maintained constant during the entire treatment even if some gas was consumed during reaction. The jars were purged several times with oxygen prior to filling to the desired pressure, which was maintained during milling. A hardened steel jar (80 cm^3 volume) and balls (9 balls, 15 mm diameter) were used in all experiments. The powder-to-ball mass ratio was set at 1:20, requiring the use of approximately 6 g of starting materials. The spinning rate of both the supporting disc and the superimposed rotation in the opposite direction of the jars was set at 700 rpm. The mechanosynthesis is carried out, nominally at room temperature, but inevitably the grinding process leads to an increase in temperature which is estimated as typically being in the range 50 to 80ºC. Some authors have proposed kinematic equations that describe the impact energy (ΔE) of the balls in the jar during milling.[61-64] This energy is transferred to the reactants in every hit and can be calculated from:

$$\Delta E = -m\left[Wv^3\,\frac{Rv-Rb}{Wp} + WpWvRp\right][Rv - Rb], \qquad (1)$$

where m is the ball mass, Wv the rotational speed of the vial, Wp the rotational speed of the supporting disk, Rv the radius of the vial and Rb the radius of the balls. In a real system, the hindering effect of the balls decreases the impact energy. The corrected impact energy, ΔE^*, considering the hindering factor (φ), is determined from: [62]

$$\Delta E^* = \varphi\,\Delta E \qquad (2)$$

The total power transferred to the sample during milling by the collisions is given by:

$$P = \Delta E^*\,N\,f \qquad (3)$$

where N is the number of balls in the jar and f is the frequency with which balls are launched, i.e. $f = K(Wp-Wv)/2\pi$, where K is a constant that depends on ball diameter and mill geometry.[63]

The weight-normalized cumulative kinetic energy released in the system (E_{cum} in J/g or Wh/g), is related to the corrected ball-impact energy, ΔE^*, the ball-impact frequency of the N balls, $v_t = NK(W_p - W_v)$, the milling time, t, and the powder weight, mp, as shown in equation 4:[64]

$$E_{cum} = \frac{\Delta E_b^* v_t t}{m_p} \qquad (4)$$

Using equations 1-4, for the milling conditions used here, the following values are obtained for the corrected impact energy and total power: ΔE^* = 82 mJ/hit and P = 25.8 W; E_{cum} is calculated from equation 4 considering the milling time required to obtain a single phase product for each composition.

Characterization

X-ray diffraction (XRD) patterns were collected with a Panalytical X'Pert Pro diffractometer working at 45 kV and 40 mA, using CuKα radiation and equipped with a X'Celerator detector and a graphite diffracted beam monochromator. The sizes of coherently diffracting domains and strains were calculated by line profile analysis (Panalytical X'Pert Pro software) corrected for instrumental peak broadening determined with a silicon standard.

The FullProf [65, 66] and Jana2006 [67] software were used for Rietveld refinement. The background was refined using a six-order polynomial function and a pseudo-Voigt with axial divergence asymmetry profile function to refine peak shapes. Peak shapes, lattice parameters, and scale were refined simultaneously. Atomic positions and isotropic temperature factors were subsequently included in the refinement.

X-ray Photoelectron Spectroscopy (XPS) was studied with a Vacuum Generator, model Escalab 210 equipment using Mg Kα radiation calibrated with the C_{1s} signal, with a pass energy resolution of 50 eV. The spectra of powder samples were recorded at room temperature under a residual pressure < 10^{-10} mbar.

Raman spectra were collected with a dispersive Horiva Jobin Yvon LabRam HR800 microscope with a 20 mW green laser (532.14 nm) and a 100× objective with a confocal pinhole of 10 µm. Microstructure of the powders was studied by scanning electron microscopy (SEM) using a Hitachi S-4800 microscope equipped with an energy dispersive X-ray spectrometer (EDAX). Differential scanning calorimetry (DSC) curves were recorded in air (100 cm^3 min^{-1}) on a simultaneous TG/DSC Instrument (Q600 SDT, TA Instruments, Crawley, UK). The experiments were performed at a heating/cooling rate of 10 ºC min^{-1} from 250ºC to 850ºC in open alumina pans.

Dilatometric measurements were recorded on pellets using a Linseis TMA model PT1000 in air at 10 ºC min^{-1} heating rate. The pellets were prepared from as-milled powders, pressed into discs, 6 mm in diameter and ~2 mm thick, by uniaxial pressing at 0.93 GPa and annealed at 850ºC.

For the electrical property measurements, pellets were prepared using the same procedure as that described for the dilatometric measurements. Opposite pellet faces were Au sputter-coated using an Emitech K575X Sputter Coater (Kent, UK). Impedance measurements used a HP 4294A impedance analyser (Wokingham, UK) over the frequency range 5 Hz to 10 MHz, with an ac measuring voltage of 0.1 V and over the temperature range ~20 to 400ºC. Impedance data were corrected for overall pellet geometry and for blank capacitance of the conductivity jig. Conductivity and permittivity data are reported in units of Scm^{-1} and Fcm^{-1}, respectively, that refer to correction for only the overall sample geometry. Density of the ceramics was determined using the Archimedes' method, using water as the immersion liquid. Pellet densities were ~ 91 %. Dielectric measurements as a function of temperature were performed using a 4263B LCR meter.

Magnetic susceptibility measurements were performed in a SQUID magnetometer (Quantum Design, model MPMS-XL) in the temperature range 2-320 K at 50 mT. The magnetic susceptibility data were collected after cooling the sample from room temperature to 2 K in a zero field (ZFC) and after cooling in the measuring field (FC). Magnetization was measured at different temperatures in magnetic field strengths up to ±5 T.

Results and discussion

Mixed oxides of general formula $Bi_{1-x}La_xFeO_3$ were prepared, over the entire range of compositions ($0 \leq x \leq 1$), by direct mechanochemical reaction of stoichiometric amounts of Bi_2O_3, Fe_2O_3 and La_2O_3 at room temperature. Fig. 1 shows the XRD patterns at periodic intervals for one composition, $Bi_{0.98}La_{0.02}FeO_3$. In the first stages of grinding, the crystallinity of the starting single oxides is damaged. After 1 hour, reflections corresponding to a new phase are detected, while those of the starting oxides are weakened. After 4 hours, the new phase appears to be phase-pure. The time required to produce a phase-pure product decreased with increasing La content from ~8 h for x = 0 to ~ 2 h for x ≥ 0.3, Fig. 2.

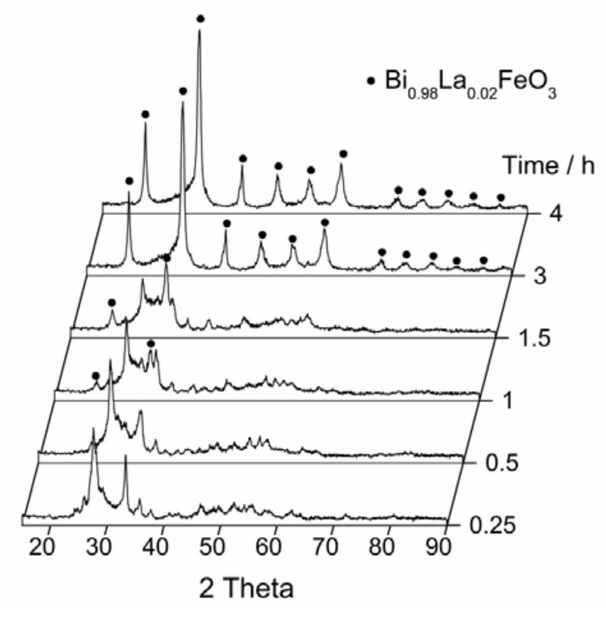

Fig. 1. Diffraction patterns obtained after milling, for different periods of time in oxygen (7 bar), stoichiometric amounts of the starting oxides for composition $Bi_{0.98}La_{0.02}FeO_3$.

The XRD peaks are broad due to the nanometric size of the crystallites obtained after milling. Similar behavior was observed for all compositions; XRD patterns at different grinding times for several compositions (ranging from x=0.07 to x=1.00) are shown in Figs. S1-S7 in the ESI†.

Fig. 2 summarizes the XRD patterns, and milling times, for final reaction products of different compositions.

The average size of the coherently diffracting domains was calculated by line profile analysis using the highest intensity single peak for each composition. Thus, for x = 0.02, 0.07 and 0.15, the peak at approximately 22.5° was used; for compositions x = 0.45, 0.60, 0.80 and 1.00, the weak peak at about 25.3° was used, as the peak at 22.5° consisted of overlapping peaks. For x = 0.30, it was not possible to calculate the crystallite size because of possible multiple peak overlap.

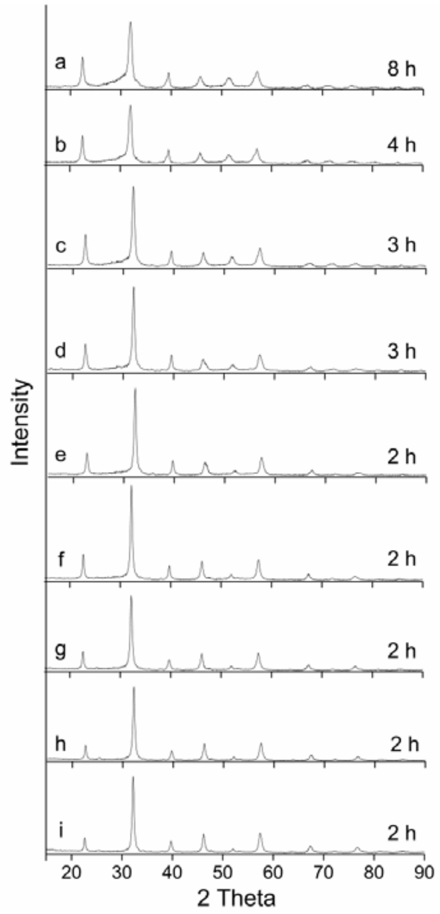

Fig. 2. XRD patterns of powders obtained after milling stoichiometric amounts of the single oxides in oxygen (7 bar) for different compositions: (a) $BiFeO_3$,[59] (b) $Bi_{0.98}La_{0.02}FeO_3$, (c) $Bi_{0.93}La_{0.07}FeO_3$, (d) $Bi_{0.85}La_{0.15}FeO_3$, (e) $Bi_{0.70}La_{0.30}FeO_3$, (f) $Bi_{0.55}La_{0.45}FeO_3$, (g) $Bi_{0.40}La_{0.60}FeO_3$, (h) $Bi_{0.20}La_{0.80}FeO_3$, (i) $LaFeO_3$. The minimum milling time for full reaction of each composition is indicated.

For each composition, crystallite size and weight-normalized cumulative kinetic energy of the milling process, *i.e.* E_{cum}, as a function of x, are shown in Fig. 3. As milling conditions were identical for every composition, the resulting E_{cum} is directly related to the time required to reach full conversion. Fig. 3a, shows that E_{cum} decreases with x from 760 kJ g^{-1}, t=8 hours, for x = 0, to 191 kJ g^{-1}, t=2 hours, for x = 0.3. This decrease in E_{cum} could be explained on the basis of increased thermodynamic stabilization of the perovskite structure produced by La substitution, as suggested by Selbach et al.[43] For x ≥ 0.3, E_{cum} remains constant at 191 kJ g^{-1}. The crystal size appears to be a function of the grinding time and, therefore, E_{cum} required for the formation of the different compositions, Fig. 3b. Larger E_{cum} required for the formation of low La content compounds yield materials with smaller crystallite sizes as they are formed under more severe mechanochemical conditions (high mechanical stresses are required for the interdiffusion of species and formation of the new phases) than those with high La content that are formed under milder conditions. The effect of longer milling times of up to 20 h on single-phase samples was studied. No changes were seen, either in the particle size of the product or their XRD patterns. There was also no evidence of any decomposition of the phases on prolonged grinding.

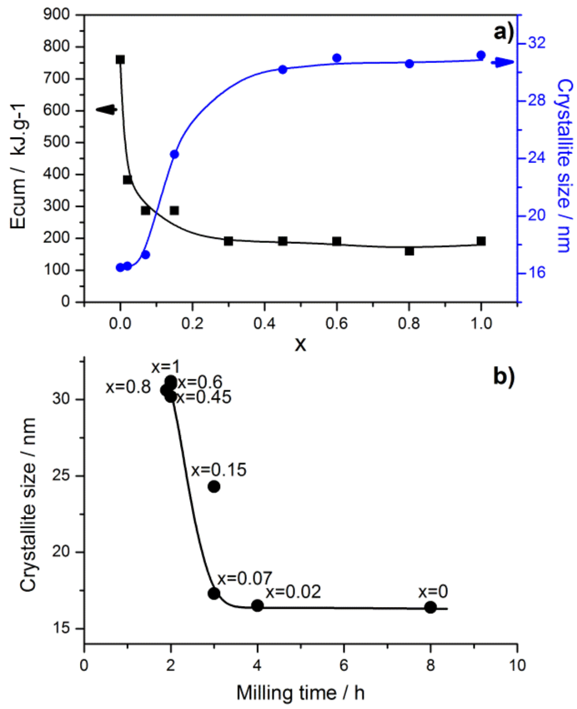

Fig. 3. (a) Crystallite size and cumulative milling kinetic energy as a function of composition. b) Crystallite size as a function of the minimum grinding time required for full conversion.

Fig. 4 includes SEM micrographs showing the morphology of ground samples of $Bi_{0.98}La_{0.02}FeO_3$ at different milling times. Initially, the products maintain the plate-like shape of Bi_2O_3 starting material. As milling continues and reaction progresses, the morphology changes to highly aggregated powders. Eventually, after four hours of treatment, when conversion was complete, the product consisted of nanometric subunits aggregated into micron-sized particles. Identical behavior has been observed for the whole set of samples prepared here (see Figs. S8-S14 in the ESI†) as well as for the mechanochemical synthesis of pure $BiFeO_3$.[59] The morphology of products as aggregates of nanoparticles is very common in materials obtained by mechanochemistry, as the mechanical energy applied causes cold welding of the nanometric subunits. Thus, the smaller is the crystal size, the higher is the concentration of grain boundaries and, therefore, the strain energy stored by the material.[68, 69] The EDX spectrum, Fig. 4d, for $Bi_{0.98}La_{0.02}FeO_3$ after 4 hours of milling shows only Bi, Fe and La. The lack of chromium indicates no relevant contamination from the hardened-steel jar and balls (again, similar results were obtained for all other compositions as shown in Figs. S8-S14 in the ESI†). Elemental compositions, as determined by EDX analysis, are shown in Table 1; results are coincident with the expected compositions, within errors.

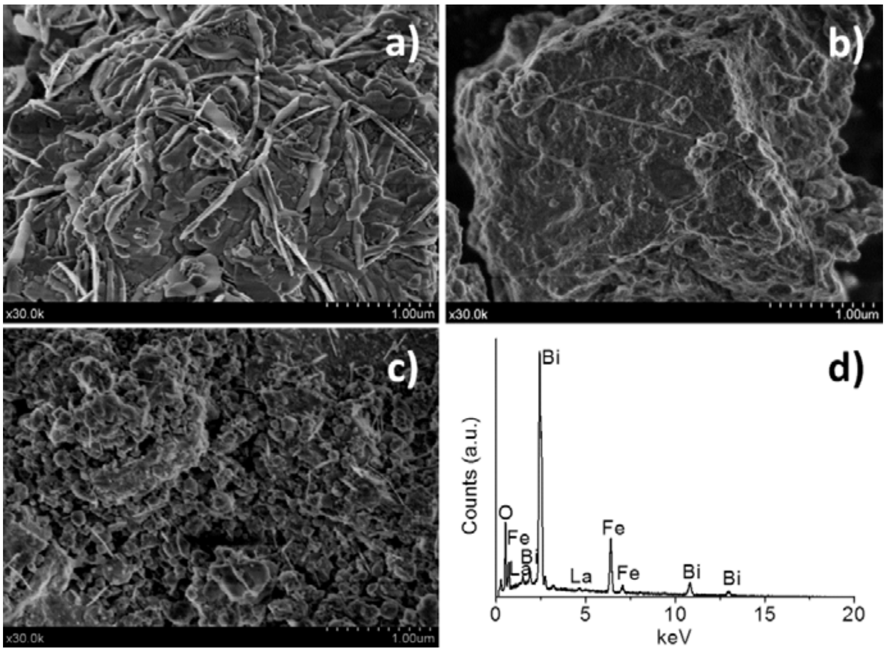

Fig. 4. SEM micrographs at different milling times for $Bi_{0.98}La_{0.02}FeO_3$: (a) 0.25 h, (b) 1 h, (c) 4 h; (d) EDX spectrum for the product obtained after 4 hours of milling shown in (c).

Table 1. Elemental composition of the powders prepared by mechanosynthesis, determined by semiquantitative analysis of EDX spectra.

Sample	Theoretical atomic composition Fe/La/Bi (%)	Experimental atomic composition Fe	La	Bi
$BiFeO_3$	50.0/0.0/50.0	50.4 ± 0.6	--	49.6 ± 0.8
$Bi_{0.98}La_{0.02}FeO_3$	50.0/1.0/49.0	50.3 ± 0.5	1.3 ± 0.3	48.4 ± 1.1
$Bi_{0.93}La_{0.07}FeO_3$	50.0/3.5/46.5	51.3 ± 0.9	3.8 ± 0.4	44.9 ± 1.8
$Bi_{0.85}La_{0.15}FeO_3$	50.0/7.5/42.5	51.5 ± 0.8	8.1 ± 0.4	40.4 ± 2.1
$Bi_{0.70}La_{0.30}FeO_3$	50.0/15.0/35.0	50.8 ± 0.8	14.8 ± 0.4	34.4 ± 1.7
$Bi_{0.55}La_{0.45}FeO_3$	50.0/22.5/27.5	50.8 ± 0.6	22.2 ± 0.5	27.1 ± 1.2
$Bi_{0.40}La_{0.60}FeO_3$	50.0/30.0/20.0	51.0 ± 1.8	29.5 ± 0.5	19.5 ± 1.1
$Bi_{0.20}La_{0.80}FeO_3$	50.0/40.0/10.0	51.0 ± 0.6	39.4 ± 1.0	9.6 ± 0.6
$LaFeO_3$	50.0/50.0/0.0	50.9 ± 0.8	49.1 ± 1.2	--

Fig. 5 shows the Fe2p, Bi4f and La3d$_{5/2}$ XPS spectra for $Bi_{0.98}La_{0.02}FeO_3$ and $LaFeO_3$. XPS is very sensitive to surface composition, providing information not only on the elements present but also on their oxidation state. As observed by EDX analysis, Cr was not detected, indicating the absence of contamination from milling media. Moreover, no oxidation states different from 3+ were detected for Bi, Fe and La. Quantitative analysis of XPS spectra yielded chemical ratios coincident with nominal compositions, suggesting that the materials prepared are chemically homogeneous.

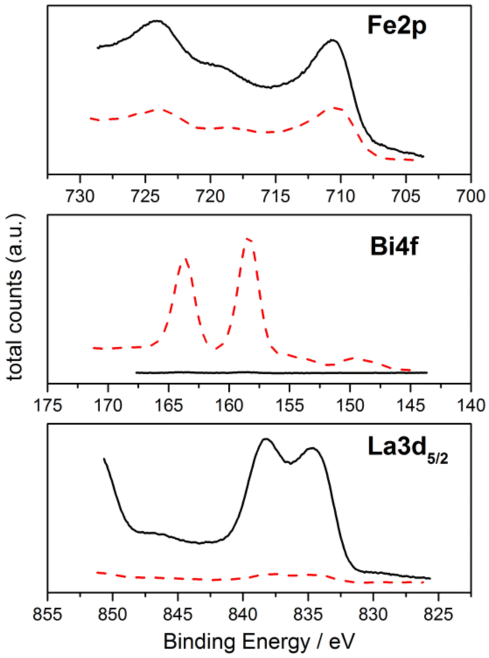

Fig. 5. XPS spectra corresponding to Fe2p, Bi4f, and La3d$_{5/2}$ for $Bi_{0.98}La_{0.02}FeO_3$ (dotted line) and $LaFeO_3$ (solid line).

The Raman spectrum of $BiFeO_3$, Fig. 6a, showed 10 lines; three can be attributed to A1 modes (at 170, 225 and 415 cm^{-1}), while the other seven are E modes (at 263, 293, 355, 372, 472, 525 and 618 cm^{-1}).[59] The bands below 200 cm^{-1} are associated with Bi-O bonds (specifically, the relative movement of cations situated in the A position of the ABO_3 structure against the BO_6 octahedron). Bands above 200 cm^{-1} are due to internal vibration of the FeO_6 octahedron: the band at 618 cm^{-1} is assigned to symmetric breathing of the oxygen atoms. The $BiFeO_3$ spectrum, Fig. 6a, is characteristic of rhombohedral $BiFeO_3$,[70] with very small discrepancies in band positions, possibly due to strain in the nanoparticles produced by mechanosynthesis.[56, 71-75] When Bi is progressively substituted by La, the Raman spectra are modified, Fig. 6, in a similar way as observed for other substituents.[76-78] Compositions $x \leq 0.15$, Fig. 6, present Raman spectra quite similar to that of pure $BiFeO_3$ (Fig. 6a) except for a small decrease in intensity of the A1 modes at low Raman shifts (below 200 cm^{-1}), associated with the decrease in number of Bi-O bonds as La content increases and, therefore, as La atoms go into Bi sites in $BiFeO_3$. For $x \geq 0.30$, the intensities of bands at low Raman shift continue to decrease, while new bands at 182 cm^{-1} and 627 cm^{-1} appear, suggesting a structural transformation as observed for other substituted $BiFeO_3$.[76, 78, 79] In general, as x increases, the Raman spectra approximate to that of pure $LaFeO_3$ (Fig. 6i).

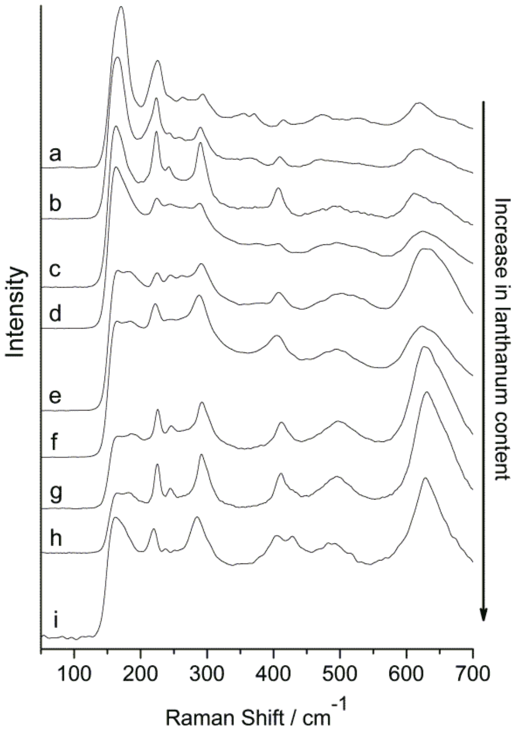

Fig. 6. Raman spectra of the powders obtained after milling stoichiometric amounts of the single oxides in oxygen (7 bar) for different compositions: (a) $BiFeO_3$, (b) $Bi_{0.98}La_{0.02}FeO_3$, (c) $Bi_{0.93}La_{0.07}FeO_3$, (d) $Bi_{0.85}La_{0.15}FeO_3$, (e) $Bi_{0.70}La_{0.30}FeO_3$, (f) $Bi_{0.55}La_{0.45}FeO_3$, (g) $Bi_{0.40}La_{0.60}FeO_3$, (h) $Bi_{0.20}La_{0.80}FeO_3$, (i) $LaFeO_3$.

The XRD patterns of mechanosynthesized samples, Fig. 2, show significant line broadening which made it difficult to obtain detailed crystallographic information. To improve crystallinity, samples were heated to 800ºC for 30 minutes, XRD patterns recorded and analyzed using the Rietveld method. An expanded section, in the range 20º to 45º 2Θ, is shown in Fig. 7. It is clear that there are structural changes for x>0.15. Thus, for x=0.30, a single peak at 22.5º splits into two peaks, while the highest intensity pair of peaks at about 32º becomes a single peak. For x > 0.45, the doublet at 22.5º again becomes a single peak and a new weak reflection at 25.3º is detected.

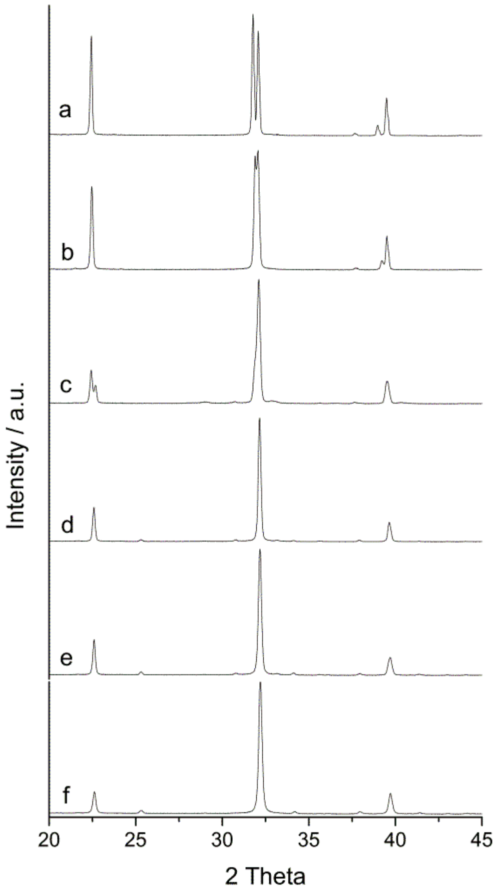

Fig. 7. XRD patterns of the powders obtained after heating at 800ºC the mechanosynthesized samples: (a) $Bi_{0.98}La_{0.02}FeO_3$, (b) $Bi_{0.85}La_{0.15}FeO_3$, (c) $Bi_{0.70}La_{0.30}FeO_3$, (d) $Bi_{0.55}La_{0.45}FeO_3$, (e) $Bi_{0.40}La_{0.60}FeO_3$, (f) $LaFeO_3$.

For compositions x=0.02, 0.07, and 0.15, XRD patterns were similar to that for x=0.00 and could be refined well in space group R3c, as shown for x=0.02 in Fig. 8 and Table 2 (see also Figs. S15-S16 in the ESI†). These results are in agreement with some of those reported for samples prepared by other methods,[9, 12, 37, 39] while other authors suggest either a change in the structure for x=0.15 or the presence of a mixture of rhombohedral and orthorhombic phases.[13, 38, 42].

Compositions x = 0.45, 0.60, 0.80 and 1.00 were refined using Pnma space group.[42, 80] The calculated diffraction patterns clearly fit the experimental data (see Figs. S17-S20 in the ESI†, and Table 2). These compositions with x ≥ 0.45 may therefore be regarded as solid solutions of $LaFeO_3$ with the same space group.

The indexing of intermediate composition, x=0.3, was tested in the space groups Imma, Pnma, $Pn2_1a$ and C222. Pnma and C222 space groups were discarded due to the very high reliability factors obtained, but refinements in Imma and $Pn2_1a$ gave similar R_{wp} values of 25.6 and 24.4 respectively. However, the diffraction pattern shows small peaks that could not be indexed with these space groups, which causes high reliability factor values. While some authors consider that these small peaks correspond to secondary phases,[37, 81] Rusakov et al. suggested, for composition x=0.25, a superspace group Imma(00γ)s00 with an incommensurate modulation vector q=0.4855(4)c*,[42] whereas Carvalho et al. proposed, for x=0.30, the superspace group $Pn2_1a$(00γ)s00 with q=0.465(1)c*.[82] It is considered that the modulation is caused by displacement of Bi and O(1) atoms along the *a* axis toward each other and by the O(2) atoms within the *ac* plane. Rietveld refinement of the superstructure in our sample, x=0.30, was carried out using Jana2006, starting with the cell parameters obtained by Fullprof software. R_{wp} values obtained in the LeBail mode for the superstructures Imma(00γ)s00 and $Pn2_1a$(00γ)s00 were 9.01 and 7.97, respectively. In particular all the small satellite peaks are fitted only by the $Pn2_1a$(00γ)s00 superstructure (see Figs. S21-S22 in the ESI†). Considering these results, a full Rietveld refinement was performed starting with the values obtained in LeBail mode for $Pn2_1a$(00γ)s00 superstructure. The calculated diffraction pattern fits the experimental, with q = 0.471(2)c* (see Fig. S23 in the ESI† and Table 2), in agreement with that obtained by Carvalho et al.[82]

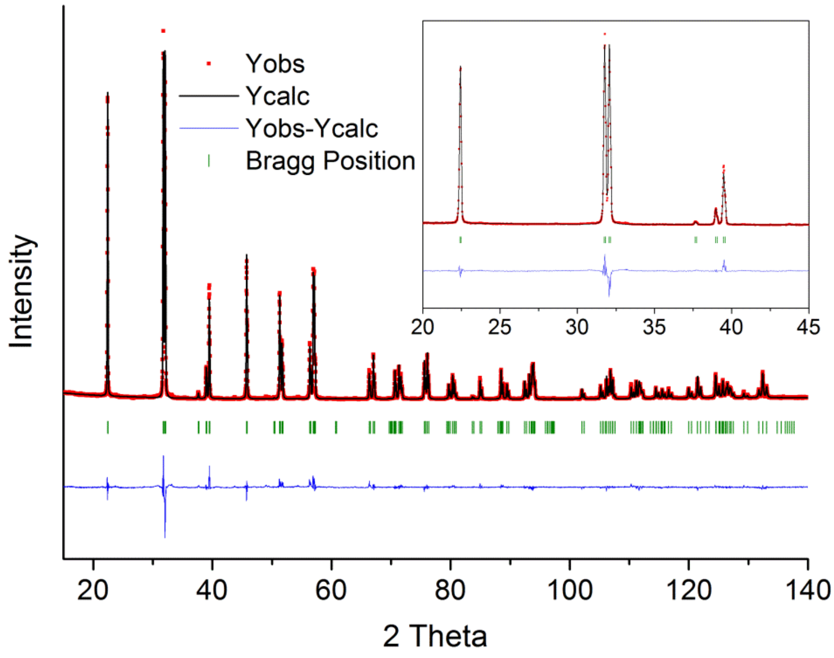

Fig. 8. XRD pattern of $Bi_{0.98}La_{0.02}FeO_3$ obtained after four hours milling and subsequent heating to 800ºC (dots). The solid lines are the fit from the Rietveld refinement. The inset shows an expanded section in the range 20º to 45º 2Θ.

Table 2. Rietveld refinement structural parameters obtained from the XRD patterns of powders of the system $Bi_{(1-x)}La_xFeO_3$ prepared by mechanosynthesis and heated to 800ºC for 30 minutes.

Sample	$Bi_{0.98}La_{0.02}FeO_3$	$Bi_{0.93}La_{0.07}FeO_3$	$Bi_{0.85}La_{0.15}FeO_3$	$Bi_{0.70}La_{0.30}FeO_3$
Space group	R3c	R3c	R3c	$Pn2_1a(00\gamma)s00$
a (Å)	5.57944(2)	5.57922(4)	5.57867(11)	5.61384(3)
b (Å)	5.57944(2)	5.57922(4)	5.57867(11)	7.83723(3)
c (Å)	13.85932(6)	13.82989(12)	13.7768(3)	5.58955(4)
Atomic positions				
Bi/La	0.00, 0.00, 0.00	0.00, 0.00, 0.00	0.00, 0.00, 0.00	0.00, 0.2580(2), 0.9875(3)
Fe	0.00, 0.00, 0.2203(5)	0.00, 0.00, 0.2226(6)	0.00, 0.00, 0.2246(5)	0.00, 0.00, 0.50
O(1)	0.4397(3), 0.0173(2), 0.9534(5)	0.4409(2), 0.0109(1), 0.9540(4)	0.4438(3), 0.0136(3), 0.9572(7)	0.5908(4), 0.2382(3), 0.0255(3)
O(2)	--	--	--	0.2481(5), 0.5365(3), 0.2541(1)
O(3)	--	--	--	0.7913(4), 0.5639(4), 0.7697(5)
Bond angle				
Fe-O(1)-Fe	154.2º	155.3º	155.9º	149.7º
Fe-O(2)-Fe	--	--	--	163.6º
Fe-O(3)-Fe	--	--	--	148.6º
Confidence factors				
χ^2, Rwp	2.53	2.62	2.92	GOF: 2.58
Rwp	13.6	15.3	16.4	13.4

Sample	$Bi_{0.55}La_{0.45}FeO_3$	$Bi_{0.40}La_{0.60}FeO_3$	$Bi_{0.20}La_{0.80}FeO_3$	$LaFeO_3$
Space group	Pnma	Pnma	Pnma	Pnma
a (Å)	5.57548(17)	5.57421(9)	5.56966(9)	5.5611(1)
b (Å)	7.8604(2)	7.86395(14)	7.85845(15)	7.8542(2)
c (Å)	5.56486(16)	5.55116(9)	5.55039(10)	5.5575(1)
Atomic positions				
Bi/La	0.0181(3), 0.25, 0.9925(4)	0.0261(2), 0.25, 0.9944(5)	0.0289(3), 0.25, 0.9939(3)	0.0279(1), 0.25, -0.0057(3)
Fe	0.00, 0.00, 0.50	0.00, 0.00, 0.50	0.00, 0.00, 0.50	0.00, 0.00, 0.50
O(1)	0.4990(4), 0.25, 0.0684(5)	0.4935(1), 0.25, 0.0752(4)	0.4901(1), 0.25, 0.0761(4)	0.4880(2), 0.25, 0.0857(5)
O(2)	0.2733(2), 0.0434(3), 0.7192(8)	0.2788(3), 0.0426(2), 0.7206(6)	0.2780(2), 0.0420(2), 0.7242(6)	0.2765(2), 0.0350(2), -0.2788(2)
Bond angle				
Fe-O(1)-Fe	158.1º	155.9º	155.5º	152.5º
Fe-O(2)-Fe	156.9º	156.7º	157.4º	159.8º
Confidence factors				
χ^2	3.92	3.28	2.28	1.49
Rwp	16.7	14.8	13.0	11.6

Fig. 9 shows the composition dependence of the normalized unit cell volume ($V Z^{-1}$) in $Bi_{1-x}La_xFeO_3$. The values were calculated from the Rietveld refinement results. Although the volume decreases as La content increases, the composition dependence is irregular, which probably reflects changes in space group as well as volume contraction associated with La substitution.

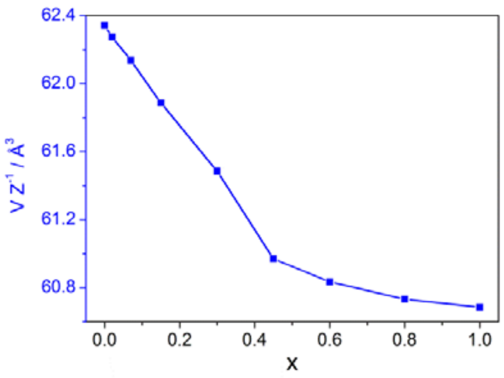

Fig. 9. Compositional dependence of the normalized unit cell volume (V Z^{-1}) in $Bi_{1-x}La_xFeO_3$.

DSC measurements illustrate the probable multiferroic character of the samples with low x. Fig. 10 shows DSC data on samples heated at 800ºC for 30 minutes. Two endotherms are seen for $x \leq 0.15$. By comparison with the reported data, and peak assignments for $BiFeO_3$, the first, weak effect corresponds to T_N (antiferromagnetic-paramagnetic transition) and the second, more intense one, to T_C (ferroelectric-paraelectric transition).[42, 49, 83, 84] For x=0.3, two endotherms are also observed, at 339.5ºC and 387.6ºC, but from the composition dependence of T_C and T_N, summarised in Fig. 11, it appears that, for x=0.30, T_C is at a lower temperature than T_N, in contrast to compositions with smaller x. Previously, the first peak at 339 ºC has been attributed to a phase transition. [42]

Relative permittivity data for x=0.30 and dilatometry data for different compositions, are shown in Fig. 12. A maximum in permittivity is seen at ~360ºC (Fig. 12a) which could indicate a ferroelectric-paraelectric transition at T_C and support the assignment of DSC peak data. Moreover, Rietveld refinement results indicate that x=0.30 exhibits the space group Pn21a(00γ)s00, which is noncentrosymmetric rather than Imma(00γ)s00, which is centrosymmetric, consistent with a ferroelectric-paraelectric transition for this composition.

The permittivity data, Fig. 12a, show a maximum at 360ºC, that continues the trend in composition dependence of T_C shown in Fig. 11, although it is noted that permittivity maxima can also be associated with antiferroelectric-paraelectric transitions. The permittivity maximum seen at 360ºC is superposed on a rapidly increasing rise in permittivity at higher temperatures; these high temperature data no longer represent bulk permittivities alone, but are increased due to interfacial polarisation effects associated with increasing levels of electronic conductivity. Dilatometric curves of dense pellets sintered at 850ºC show no changes at T_N, but significant volume reduction at T_C, especially for low x compositions; for x=0.30, a small inflection at ~360ºC is seen, Fig. 12b. The more gradual decrease in volume seen at the highest temperatures may be associated with sample sintering, perhaps enhanced by compaction of the sample following the phase transition at T_C for samples $x \leq 0.15$, but in particular, because these temperatures are close to the melting temperatures (933ºC for $BiFeO_3$; data for La-doped $BiFeO_3$ are not available).

In the tentative phase diagram for the system $Bi_{(1-x)}La_xFeO_3$ in Fig. 11, the ferroic transition sequences may be identified. With increasing temperature, these are:

(i) $x<0.28$, antiferromagnetic + ferroelectric → paramagnetic + ferroelectric → paramagnetic + paraelectric.

(ii) $0.28 < x < 0.45$, antiferromagnetic + ferroelectric or antiferroelectric → antiferromagnetic + paraelectric → paramagnetic + paraelectric.

(iii) $x \geq 0.45$, antiferromagnetic + paraelectric → paramagnetic + paraelectric.

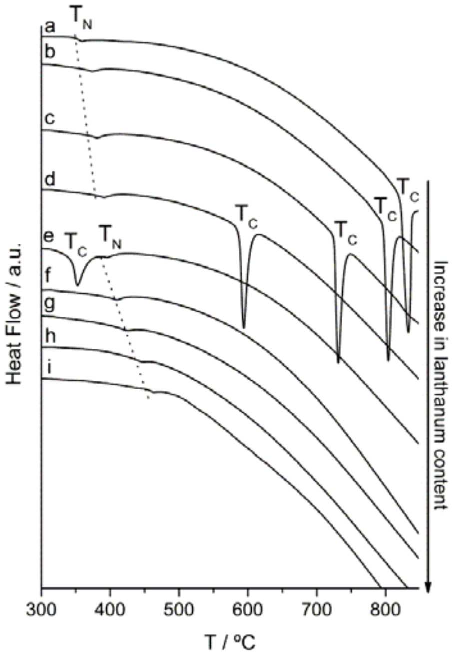

Fig. 10. DSC diagrams obtained for mechanosynthesized samples after heating at 800ºC: (a) $BiFeO_3$, (b) $Bi_{0.98}La_{0.02}FeO_3$, (c) $Bi_{0.93}La_{0.07}FeO_3$, (d) $Bi_{0.85}La_{0.15}FeO_3$, (e) $Bi_{0.70}La_{0.30}FeO_3$, (f) $Bi_{0.55}La_{0.45}FeO_3$, (g) $Bi_{0.40}La_{0.60}FeO_3$, (h) $Bi_{0.20}La_{0.80}FeO_3$, (i) $LaFeO_3$. The dotted line linking T_N is a guide to the eye.

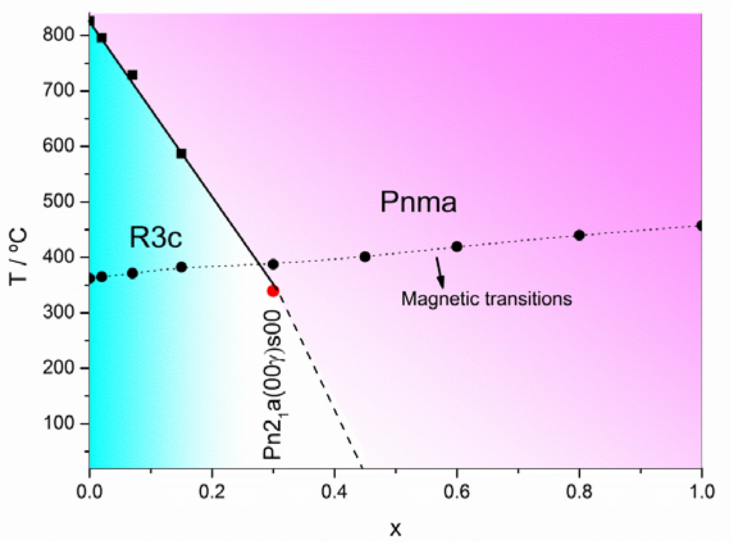

Fig. 11. Phase diagram for the system $Bi_{1-x}La_xFeO_3$. The compositional dependence of the Néel (T_N) and Curie (T_C) temperatures obtained from the DSC traces shown in Fig. 10.

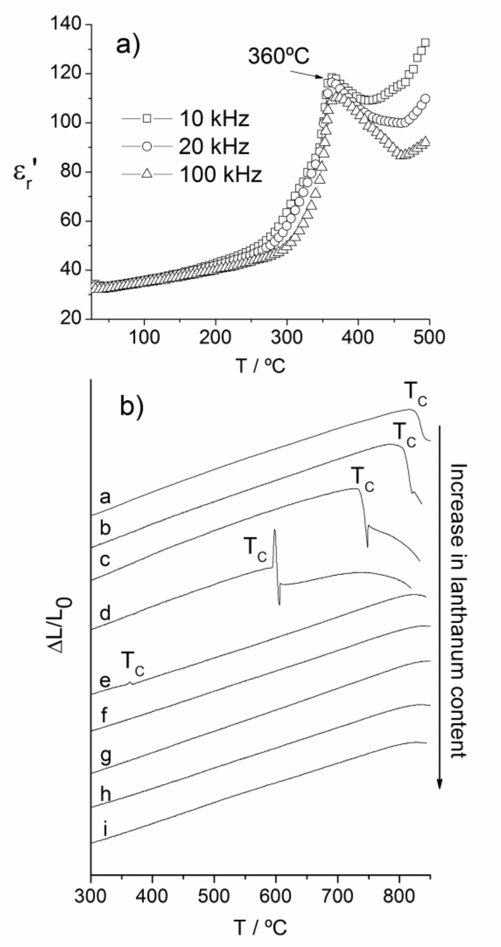

Fig. 12. (a) Relative permittivity (ε_r') as a function of temperature at different frequencies for $Bi_{0.70}La_{0.30}FeO_3$. An anomaly is observed with a maximum at 360ºC. (b) Dilatometric curves of dense pellets (>90%) prepared by sintering at 850ºC the samples obtained after milling stoichiometric amounts of the single oxides in oxygen (7 bar) for: (a) $BiFeO_3$, (b) $Bi_{0.98}La_{0.02}FeO_3$, (c) $Bi_{0.93}La_{0.07}FeO_3$, (d) $Bi_{0.85}La_{0.15}FeO_3$, (e) $Bi_{0.70}La_{0.30}FeO_3$, (f) $Bi_{0.55}La_{0.45}FeO_3$, (g) $Bi_{0.40}La_{0.60}FeO_3$, (h) $Bi_{0.20}La_{0.80}FeO_3$, (i) $LaFeO_3$.

High temperature powder XRD patterns for $Bi_{0.85}La_{0.15}FeO_3$ are shown in Fig. 13 for three temperatures on stepwise heating and subsequently on cooling to room temperature. The patterns at room temperature and 400ºC are essentially identical, indicating no noticeable change in crystal structure when heated above T_N, as expected for an antiferromagnetic-paramagnetic transition that implies only a change in magnetic order. These results agree with the DSC and dilatometric data presented above, showing that the Néel transition is endothermic, but does not involve any change in the sample dimensions. The XRD pattern at 650ºC, above T_C, is different to those at lower temperatures and was indexed in the orthorhombic space group Pnma (Fig. 11), but the transition is reversible on cooling, also in agreement with the DSC and dilatometric results, showing that the Curie transition is endothermic with a significant change in sample dimensions; the reversibility of both transitions was observed by DSC (not shown). Similar high temperature XRD results were obtained for x=0.30 (see Fig. S24 in the ESI†), but the XRD pattern changed at ~ 350ºC, similar to the T_C value obtained by DSC, and was also indexed in space group Pnma, Fig. 11.

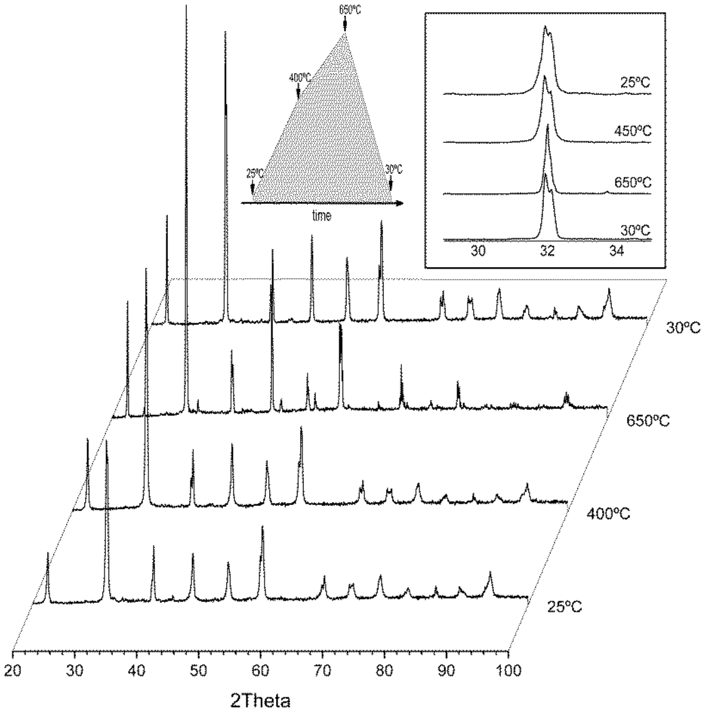

Fig. 13. In situ X-ray diffraction patterns of x=0.15 at different temperatures; the heating profile is included as an inset, with the recording temperatures marked. The second inset gives the range 29-35º on expanded scale

Impedance measurements were made, as a function of temperature, for samples in the range $0 \leq x \leq 0.15$. All samples were highly insulating at room temperature with resistivity >> 10^7 Ωcm but showed modest levels of semiconductivity at high temperatures; a typical impedance complex plane plot, Fig. 14(a), for x = 0.15, shows a single arc, but somewhat distorted from the ideal semicircular shape; the associated Z"/M" spectroscopic plots, Fig. 14(b), show single peaks with some broadening and a small difference in peak maxima frequencies. These results show that the mechanosynthesised ceramics are, essentially, electrically homogeneous with no evidence of more resistive grain boundaries/surface layers, as shown by the absence of any additional peaks at lower frequencies in the Z'' spectrum, Fig. 14(b).

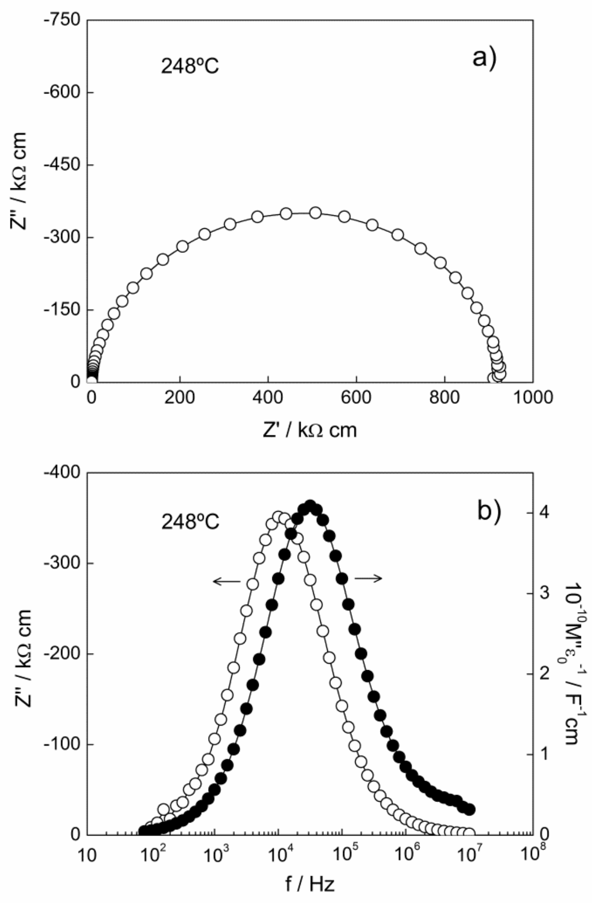

Fig. 14. (a) Impedance complex plane and (b) Z"/M" spectroscopic plots for $Bi_{0.85}La_{0.15}FeO_3$.

Resistivity values obtained from intercepts on the real, Z' axis are shown in conventional Arrhenius format in Fig. 15. Conductivity data exhibit linear behavior with activation energy ~1.14–1.20 eV; the bulk resistivity at room temperature, extrapolated from the high temperature data, is ~ 7 × 10^{16} – 8 × 10^{14} Ωcm. The conductivity increases with x but the activation energies are comparable indicating an increase in number of charge carriers with x, although the conductivity values are small, as reported earlier for stoichiometric $BiFeO_3$,[59] and are several orders of magnitude less than those reported by other groups on samples prepared by solid state reaction. The low conductivity of our samples implies that there are no significant sources of conductivity, such as mixed valence of Fe associated with possible oxygen non-stoichiometry. This may be a consequence of first, the oxygen pressure, 7 bars, that was maintained during mechanosynthesis, and second, the relatively low temperature used in synthesis (nominally room temperature, but inevitably some temperature increase associated with the milling process). One of the major objectives in the fabrication of $BiFeO_3$-related materials is to reduce the conductivity and this has been achieved in our samples prepared by mechanosynthesis.

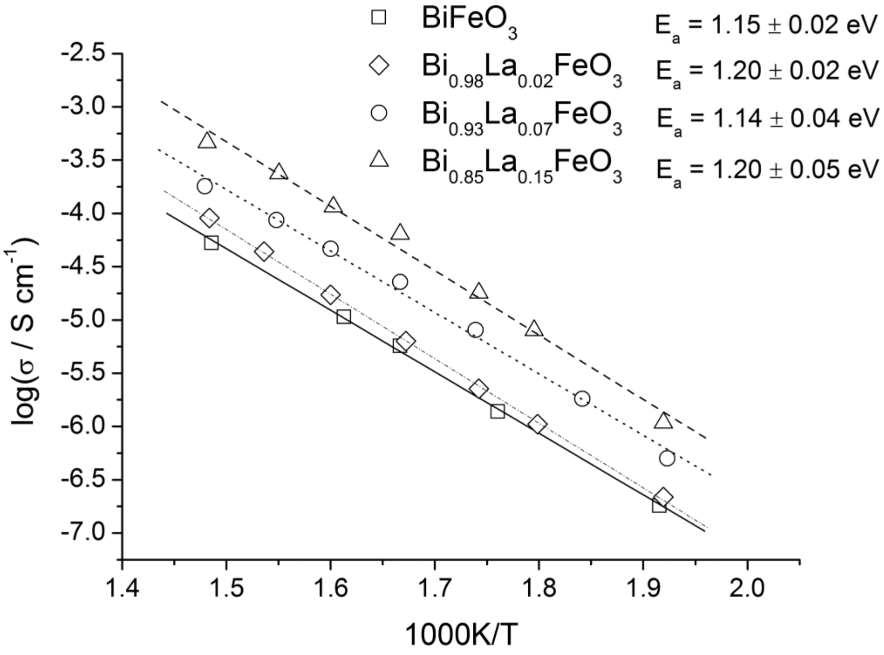

Fig. 15. Bulk conductivity data for $Bi_{1-x}La_xFeO_3$ ceramics.

The conduction mechanism was shown to be p-type electronic by measurements of the impedance in atmospheres of different oxygen partial pressure, as shown for x = 0.15 sintered at

850ºC and measured at 400ºC in Fig. 16. This means that samples pick up O_2 by the nominal mechanism:

$$O_2 \rightarrow 2O^{2-} + 4h^{\bullet} \qquad (5)$$

The origin of the holes is not known. One possibility could be Fe^{3+} ions, near the sample surface, that ionise to Fe^{4+}: the ionised electrons would be trapped at adsorbed surface oxide ions, equation 5, and the holes associated with Fe^{4+} become the principal charge carriers. Nevertheless, Fe^{4+} was not detected by XPS measurements; another possibility is that underbonded surface oxide ions may ionise:

$$O^{2-} \rightarrow O^{-} + e^{-} \qquad (6)$$

and the resulting O^- ions become the source of holes. The possible existence of O^- ions is rarely considered in electroceramic materials, but several examples of its likely existence, and contribution to p-type conduction, have been reported in acceptor-doped $BaTiO_3$, $SrTiO_3$ and $CaTiO_3$.[85, 86] The increase in hole concentration, Fig 15, is consistent with a reduction in unit cell volume, Fig. 9, and a reduction in size of oxygen anions associated with equation (6), with increasing x.

The results shown in Fig 16 are sufficient to identify holes as the principal charge carrier and to permit discussion of the location of the holes, on either Fe or O. Further information on the charge compensation mechanism would require many more data points, as a function of pO_2, than are shown in Fig 16.

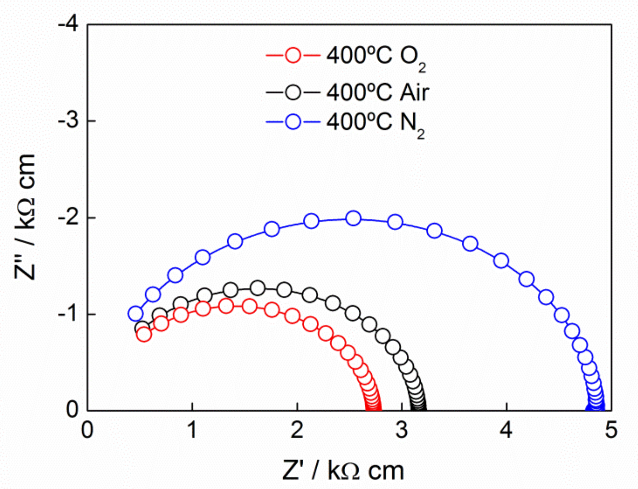

Fig. 16. Impedance complex-plane plots at 400ºC in air, oxygen and nitrogen for $Bi_{0.85}La_{0.15}FeO_3$.

Electrical polarisation (P) vs electric field (E) hysteresis loops at room temperature for x=0.15 are shown in Fig 17. There is no evidence of saturation in the P-E loop up to the maximum electric fields available in our experimental setup. Undoped $BiFeO_3$ is ferroelectric and shows switching behavior in the hysteresis loops provided the applied fields are higher than the coercive field.

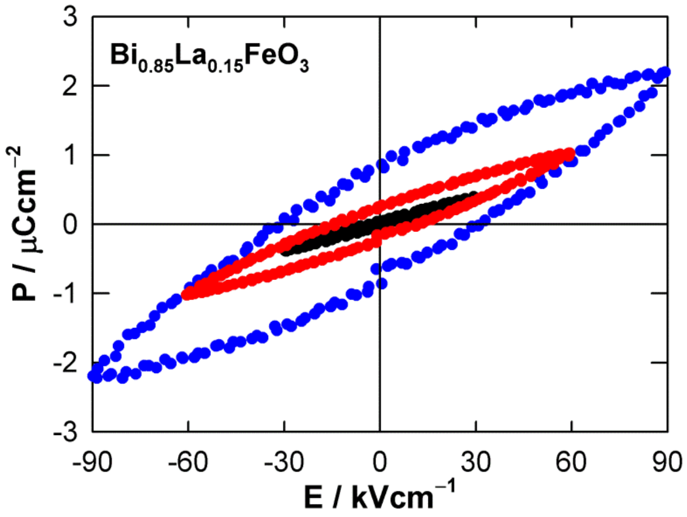

Fig. 17. Polarisation (P) vs electric field (E) hysteresis loops at room temperature for x=0.15.

The results shown in Fig. 17 indicate local movements of the domain walls but they are pinned too strongly to permit domain switching.[87] Further work is required to determine whether the coercive field varies with composition as T_C decreseases with x; alternatively, quenching samples from high temperatures may release the defects that act as domain wall pinning centers, as has been reported for samples in the $BiFeO_3$-$PbTiO_3$ system.[88]

Magnetization measurements of the mechanosynthesised powders were carried out in the ZFC and FC modes from 2 to 230 K with an applied magnetic field of 50 mT. Results for $BiFeO_3$[60] and $Bi_{0.98}La_{0.02}FeO_3$ presented in Fig. 18 show hysteresis between ZFC and FC magnetization, which is indicative of the presence of a ferromagnetic contribution. Magnetization vs. H plots at 5 and 300 K (see Fig. 25 in the ESI†), confirm the proposed behavior; the hysteresis loop obtained at room temperature shows a very weak hysteresis corresponding to the antiferromagnetic behavior with an intrinsic canting of the $BiFeO_3$, while the magnetization vs. H plot at 5 K shows a larger hysteresis due to nanoparticles behaving as ferromagnetic ones. The diamagnetic A-site substitution in $Bi_{1-x}A_xFeO_3$ has been found to be an effective method to suppress the spiral spin structure of $BiFeO_3$. In this sense, Fig. 18b shows the evolution of the magnetic susceptibility for $Bi_{0.98}La_{0.02}FeO_3$; the ZFC and FC curves converge around 320 K which can be identified as the blocking temperature, T_B. This high value of T_B agrees with the results obtained for $BiFeO_3$ nanoparticles, Fig 18a; simultaneously, an enhancement in magnetic susceptibility is observed over the entire range of temperatures, as has been reported by other authors.[13, 89]

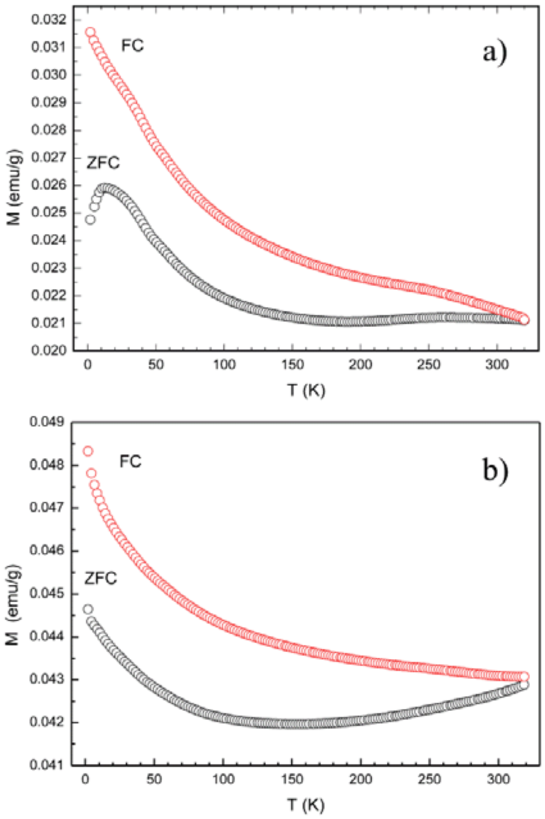

Fig. 17. Temperature dependence of zero-field cooled (ZFC) and field cooled (FC) magnetization measured with an applied magnetic field (H) of 50 mT for (a) $BiFeO_3$ and (b) $Bi_{0.98}La_{0.02}FeO_3$.

Table 3 summarizes the results obtained for magnetic hysteresis loops of samples with $x \leq 0.15$, measured at 300 K (see Fig. 26 in the ESI†). All samples show a nearly linear field-dependent magnetization and do not saturate at the maximum field attainable, H = 5T, as has been observed by other authors for mechanosynthesized $BiFeO_3$ nanoparticles.[55] Magnetization at 5T (M_{5T}) is quite similar for samples x = 0 and x = 0.15, but a small decrease in M_{5T} is observed for x = 0.02 and x = 0.07. The values of M_{5T} are influenced by two parameters, the particle size and lanthanum content. An enhanced magnetization has already been reported as particle size decreases in $BiFeO_3$ nanoparticles and is related in small antiferromagnetic particles with uncompensated spins to a small contribution at the surface.[90-92] A similar effect has been attributed, with increasing lanthanum content, to destruction of the cycloid spin-structure in $BiFeO_3$ and distortion of the crystal structure on La substitution.[13, 46, 89] Therefore, in our samples, the lower value of M_{5T} for x = 0.02 compared with $BiFeO_3$ could be explained by considering that the effect of particle size dominates the magnetization. For x = 0.07 and x = 0.15, the magnetization increases because, despite the increase in particle size, the effect of increased La content dominates the magnetization. For low values of x, the La substitution suppresses but does not destroy the spin cycloid completely, resulting in a limited increase of magnetization.[89] Remanent magnetization increases with x, independent of particle size, revealing increased suppression of the spin cycloid structure.[13, 49, 93] The big increase in coercive field of the La-substituted samples implies that the magnetic anisotropy also increases.[9, 21, 93]

Table 3. Values of the magnetization at 5 T (M_{5T}), remanent magnetization (M_r) and coercive magnetic field (H_c) obtained from hysteresis loops measured at 300 K for $Bi_{1-x}La_xFeO_3$: x= 0, 0.02, 0.07 and 0.15.

Sample	M_{5T} (emu/g)	M_r (emu/g)	H_c (Oe)
$BiFeO_3$	0.587	3.06×10^{-2}	~ 600
$Bi_{0.98}La_{0.02}FeO_3$	0.504	3.36×10^{-2}	~ 2200
$Bi_{0.93}La_{0.07}FeO_3$	0.541	5.12×10^{-2}	~ 3200
$Bi_{0.85}La_{0.15}FeO_3$	0.585	6.32×10^{-2}	~ 2800

Conclusions

Mechanosynthesis is a valuable procedure for the preparation of high quality $Bi_{1-x}La_xFeO_3$ solid solutions covering the whole compositional range. The materials prepared are chemically homogeneous as suggested by bulk (EDX) and surface (XPS) chemical analysis, impedance spectroscopy and magnetization measurements. Lanthanum content plays an important role in the kinetics of the mechanochemical reaction. Thus, as the amount of lanthanum increases, the rate of formation of the final phases also increases up to x=0.3, while for larger lanthanum contents, the reaction rate seems to be unaffected. With increasing x, milling time required for obtaining final phases is reduced and the crystallite size of the final product increases. This may reflect the increased thermodynamic stability of the solid solutions with increasing x. Lanthanum content determines the crystallographic structure of the final phases, as assayed by Raman spectroscopy and X-ray diffraction analysis, including Rietveld analysis. For x≤0.15, the space group is R3c and for x≥0.45 is Pnma; for intermediate composition x=0.3, the non-centrosymetric Pn21a(00γ)s00 super structure is obtained. The multiferroic character of the samples with compositions in the range of $x \leq 0.30$ is described by the two transitions detected at high temperatures, i.e. antiferromagnetic-paramagnetic transition at T_N and ferroelectric-paraelectric transition at T_C. The former transition involves a change in magnetic order and does not involve any modification in crystal structure, while the latter one involves a change in the structure. Impedance spectroscopy measurements show that the samples are electrically homogeneous, with low conductivity that increases with x, and a p-type conduction mechanism. Magnetic measurements confirm the high quality of the $Bi_{1-x}La_xFeO_3$ nanoparticles, and reveal the combined effect of particle size and La content on the magnetization values.

Acknowledgements

Financial support from project CTQ2011-27626 (Spanish Ministerio de Economía y Competitividad), Junta de Andalucía (TEP-7858) and FEDER funds are acknowledged. Additionally, one of the authors (PESJ) is supported by a Juan de la Cierva grant.

† **Electronic supplementary information (ESI) available:** XRD patterns, SEM micrographs and EDX spectra of the mechanosynthetized samples; Rietveld refinements; high temperature powder XRD patterns for $Bi_{0.70}La_{0.30}FeO_3$; Magnetization vs. H plots obtained at 5 and 300 K for $BiFeO_3$ nanoparticles.

References

1. H. Schmid, *Ferroelectrics*, 1994, **162**, 1, 317-338.
2. W. Eerenstein, N. D. Mathur and J. F. Scott, *Nature*, 2006, **442**, 7104, 759-765.
3. N. A. Spaldin and M. Fiebig, *Science*, 2005, **309**, 5733, 391-392.
4. A. Roy, R. Gupta and A. Garg, *Advances in Condensed Matter Physics*, 2012, 926290.
5. G. Catalan and J. F. Scott, *Advanced Materials*, 2009, **21**, 24, 2463-2485.
6. C. Ederer and N. A. Spaldin, *Physical Review B*, 2005, **71**, 6, 060401.
7. J. M. Moreau, C. Michel, R. Gerson and W. J. James, *Journal of Physics and Chemistry of Solids*, 1971, **32**, 6, 1315-1320.
8. M. Valant, A. K. Axelsson and N. Alford, *Chemistry of Materials*, 2007, **19**, 22, 5431-5436.
9. S. R. Das, R. N. P. Choudhary, P. Bhattacharya, R. S. Katiyar, P. Dutta, A. Manivannan and M. S. Seehra, *Journal of Applied Physics*, 2007, **101**, 3, 034104.
10. I. P. Sosnowska, R., *Physical review. B*, 2011, **84**, 14, 1098-10121.
11. D. Lebeugle, D. Colson, A. Forget, M. Viret, P. Bonville, J. F. Marucco and S. Fusil, *Physical Review B*, 2007, **76**, 2, 024116.

12. F. G. Garcia, C. S. Riccardi and A. Z. Simoes, *Journal of Alloys and Compounds*, 2010, **501**, 1, 25-29.
13. Z. X. Cheng, A. H. Li, X. L. Wang, S. X. Dou, K. Ozawa, H. Kimura, S. J. Zhang and T. R. Shrout, *Journal of Applied Physics*, 2008, **103**, 7, 07e507.
14. G. Catalan, K. Sardar, N. S. Church, J. F. Scott, R. J. Harrison and S. A. T. Redfern, *Physical Review B*, 2009, **79**, 21, 212415.
15. Y. F. Cui, Y. G. Zhao, L. B. Luo, J. J. Yang, H. Chang, M. H. Zhu, D. Xie and T. L. Ren, *Applied Physics Letters*, 2010, **97**, 22, 222904.
16. J. Dhahri, M. Boudard, S. Zemni, H. Roussel and M. Oumezzine, *Journal of Solid State Chemistry*, 2008, **181**, 4, 802-811.
17. Y. K. Jun, W. T. Moon, C. M. Chang, H. S. Kim, H. S. Ryu, J. W. Kim, K. H. Kim and S. H. Hong, *Solid State Communications*, 2005, **135**, 1-2, 133-137.
18. V. A. Khomchenko, D. A. Kiselev, J. M. Vieira, L. Jian, A. L. Kholkin, A. M. L. Lopes, Y. G. Pogorelov, J. P. Araujo and M. Maglione, *Journal of Applied Physics*, 2008, **103**, 2, 024105.
19. D. Kothari, V. R. Reddy, A. Gupta, D. M. Phase, N. Lakshmi, S. K. Deshpande and A. M. Awasthi, *Journal of Physics-Condensed Matter*, 2007, **19**, 13, 136202.
20. M. Kumar and K. L. Yadav, *Applied Physics Letters*, 2007, **91**, 11, 112911.
21. G. Le Bras, D. Colson, A. Forget, N. Genand-Riondet, R. Tourbot and P. Bonville, *Physical Review B*, 2009, **80**, 13, 134417.
22. J. Liu, L. Fang, F. G. Zheng, S. Ju and M. R. Shen, *Applied Physics Letters*, 2009, **95**, 2, 022511.
23. D. Maurya, H. Thota, A. Garg, B. Pandey, P. Chand and H. C. Verma, *Journal of Physics-Condensed Matter*, 2009, **21**, 2, 026007.
24. R. Mazumder and A. Sen, *Journal of Alloys and Compounds*, 2009, **475**, 1-2, 577-580.
25. S. K. Pradhan, J. Das, P. P. Rout, S. K. Das, D. K. Mishra, D. R. Sahu, A. K. Pradhan, V. V. Srinivasu, B. B. Nayak, S. Verma and B. K. Roul, *Journal of Magnetism and Magnetic Materials*, 2010, **322**, 22, 3614-3622.
26. F. Z. Qian, J. S. Jiang, S. Z. Guo, D. M. Jiang and W. G. Zhang, *Journal of Applied Physics*, 2009, **106**, 8, 084312.
27. Reetu, A. Agarwal, S. Sanghi and Ashima, *Journal of Applied Physics*, 2011, **110**, 7, 073909.
28. P. Uniyal and K. L. Yadav, *Materials Letters*, 2008, **62**, 17-18, 2858-2861.
29. D. Varshney, A. Kumar and K. Verma, *Journal of Alloys and Compounds*, 2011, **509**, 33, 8421-8426.
30. D. H. Wang, W. C. Goh, M. Ning and C. K. Ong, *Applied Physics Letters*, 2006, **88**, 21, 212907.
31. L. Y. Wang, D. H. Wang, H. B. Huang, Z. D. Han, Q. Q. Cao, B. X. Gu and Y. W. Du, *Journal of Alloys and Compounds*, 2009, **469**, 1-2, 1-3.
32. Z. Yan, K. F. Wang, J. F. Qu, Y. Wang, Z. T. Song and S. L. Feng, *Applied Physics Letters*, 2007, **91**, 8, 082906.
33. C. H. Yang, J. Seidel, S. Y. Kim, P. B. Rossen, P. Yu, M. Gajek, Y. H. Chu, L. W. Martin, M. B. Holcomb, Q. He, P. Maksymovych, N. Balke, S. V. Kalinin, A. P. Baddorf, S. R. Basu, M. L. Scullin and R. Ramesh, *Nature Materials*, 2009, **8**, 6, 485-493.
34. X. L. Yu and X. Q. An, *Solid State Communications*, 2009, **149**, 17-18, 711-714.
35. A. V. Zalesskii, A. A. Frolov, T. A. Khimich and A. A. Bush, *Physics of the Solid State*, 2003, **45**, 1, 141-145.
36. M. Polomska, Kaczmare.W and Z. Pajak, *Physica Status Solidi a-Applied Research*, 1974, **23**, 2, 567-574.
37. I. O. Troyanchuk, M. V. Bushinsky, D. V. Karpinsky, O. S. Mantytskaya, V. V. Fedotova and O. I. Prochnenko, *physica status solidi (b)*, 2009, **246**, 8, 1901-1907.

38. G. L. Yuan, K. Z. Baba-Kishi, J. M. Liu, S. Wing Or, Y. P. Wang and Z. G. Liu, *Journal of the American Ceramic Society*, 2006, **89**, 10, 3136-3139.
39. Q. H. Jiang, C. W. Nan and Z. J. Shen, *Journal of the American Ceramic Society*, 2006, **89**, 7, 2123-2127.
40. G. L. Yuan, S. W. Or and H. L. W. Chan, *Journal of Physics D-Applied Physics*, 2007, **40**, 4, 1196-1200.
41. S. T. Zhang, Y. Zhang, M. H. Lu, C. L. Du, Y. F. Chen, Z. G. Liu, Y. Y. Zhu, N. B. Ming and X. Q. Pan, *Applied Physics Letters*, 2006, **88**, 16, 162901.
42. D. A. Rusakov, A. M. Abakumov, K. Yamaura, A. A. Belik, G. Van Tendeloo and E. Takayama-Muromachi, *Chemistry of Materials*, 2011, **23**, 2, 285-292.
43. S. M. Selbach, M. A. Einarsrud and T. Grande, *Chemistry of Materials*, 2009, **21**, 1, 169-173.
44. R. D. Shannon, *Acta Crystallographica Section A*, 1976, **32**, SEP1, 751-767.
45. Q. Zhang, X. Zhu, Y. Xu, H. Gao, Y. Xiao, D. Liang, J. Zhu, J. Zhu and D. Xiao, *Journal of Alloys and Compounds*, 2013, **546**, 57-62.
46. Y. Du, Z. X. Cheng, M. Shahbazi, E. W. Collings, S. X. Dou and X. L. Wang, *Journal of Alloys and Compounds*, 2010, **490**, 1-2, 637-641.
47. R. Rai, S. K. Mishra, N. K. Singh, S. Sharma and A. L. Kholkin, *Current Applied Physics*, 2011, **11**, 3, 508-512.
48. P. Pandit, S. Satapathy and P. K. Gupta, *Physica B: Condensed Matter*, 2011, **406**, 13, 2669-2677.
49. X. Yan, J. Chen, Y. Qi, J. Cheng and Z. Meng, *Journal of the European Ceramic Society*, 2010, **30**, 2, 265-269.
50. P. Balaz, M. Achimovicova, M. Balaz, P. Billik, Z. Cherkezova-Zheleva, J. M. Criado, F. Delogu, E. Dutkova, E. Gaffet, F. J. Gotor, R. Kumar, I. Mitov, T. Rojac, M. Senna, A. Streletskii and K. Wieczorek-Ciurowa, *Chemical Society Reviews*, 2013, **42**, 18, 7571-7637.
51. L. Takacs, *Chemical Society Reviews*, 2013, **42**, 18, 7649-7659.
52. C. Correas, T. Hungria and A. Castro, *Journal of Materials Chemistry*, 2011, **21**, 9, 3125-3132.
53. D. Maurya, H. Thota, K. S. Nalwa and A. Garg, *Journal of Alloys and Compounds*, 2009, **477**, 1-2, 780-784.
54. A. A. Cristobal and P. M. Botta, *Materials Chemistry and Physics*, 2013, **139**, 2-3, 931-935.
55. K. L. Da Silva, D. Menzel, A. Feldhoff, C. Kubel, M. Bruns, A. Paesano, A. Duvel, M. Wilkening, M. Ghafari, H. Hahn, F. J. Litterst, P. Heitjans, K. D. Becker and V. Sepelak, *Journal of Physical Chemistry C*, 2011, **115**, 15, 7209-7217.
56. I. Szafraniak, M. Polomska, B. Hilczer, A. Pietraszko and L. Kepinski, *Journal of the European Ceramic Society*, 2007, **27**, 13-15, 4399-4402.
57. V. F. Freitas, H. L. C. Grande, S. N. de Medeiros, I. A. Santos, L. F. Cótica and A. A. Coelho, *Journal of Alloys and Compounds*, 2008, **461**, 1-2, 48-52.
58. A. Moure, J. Tartaj and C. Moure, *Journal of Alloys and Compounds*, 2011, **509**, 25, 7042-7046.
59. A. Perejon, N. Maso, A. R. West, P. E. Sanchez-Jimenez, R. Poyato, J. M. Criado and L. A. Perez-Maqueda, *Journal of the American Ceramic Society*, 2013, **96**, 4, 1220-1227.
60. A. Perejon, N. Murafa, P. E. Sanchez-Jimenez, J. M. Criado, J. Subrt, M. J. Dianez and L. A. Perez-Maqueda, *Journal of Materials Chemistry C*, 2013, **1**, 22, 3551-3562.
61. M. Abdellaoui and E. Gaffet, *Acta Metallurgica et Materialia*, 1995, **43**, 3, 1087-1098.
62. N. Burgio, A. Iasonna, M. Magini, S. Martelli and F. Padella, *Nuovo Cimento Della Societa Italiana Di Fisica D-Condensed Matter Atomic Molecular and Chemical Physics Fluids Plasmas Biophysics*, 1991, **13**, 4, 459-476.

63. M. Magini, C. Colella, A. Iasonna and F. Padella, *Acta Materialia*, 1998, **46**, 8, 2841-2850.
64. T. Rojac, M. Kosec, B. Malič and J. Holc, *Journal of the European Ceramic Society*, 2006, **26**, 16, 3711-3716.
65. H. M. Rietveld, *Journal of Applied Crystallography*, 1969, **2**, 65-71.
66. J. Rodriguez-Carvajal, *Short Reference Guide of the FullProf. Prog., Version 3.5, Laboratory Leon Brilloium (CEA-CNRS)*, 1997.
67. V. Petricek, Dusek,M., Palatinus,L., *Jana2006. The crystallographic computing system. Institute of Physics, Praha, Czech Republic*, 2006.
68. J. M. Criado, M. Gonzalez and C. Real, *Journal of Materials Science Letters*, 1986, **5**, 4, 467-469.
69. M. D'Incau, M. Leoni and P. Scardi, *Journal of Materials Research*, 2007, **22**, 6, 1744-1753.
70. R. Palai, R. S. Katiyar, H. Schmid, P. Tissot, S. J. Clark, J. Robertson, S. A. T. Redfern, G. Catalan and J. F. Scott, *Physical Review B*, 2008, **77**, 1, 014110.
71. J. M. Criado and J. M. Trillo, *Journal of the Chemical Society-Faraday Transactions I*, 1975, **71**, 4, 961-966.
72. H. Fukumura, H. Harima, K. Kisoda, M. Tamada, Y. Noguchi and M. Miyayama, *Journal of Magnetism and Magnetic Materials*, 2007, **310**, 2, E367-E369.
73. D. Kothari, V. R. Reddy, V. G. Sathe, A. Gupta, A. Banerjee and A. M. Awasthi, *Journal of Magnetism and Magnetic Materials*, 2008, **320**, 3-4, 548-552.
74. M. K. Singh, H. M. Jang, S. Ryu and M.-H. Jo, *Applied Physics Letters*, 2006, **88**, 4, 042907.
75. G. L. Yuan, S. W. Or and H. L. W. Chan, *Journal of Applied Physics*, 2007, **101**, 6, 064101.
76. A. Gautam, K. Singh, K. Sen, R. K. Kotnala and M. Singh, *Materials Letters*, 2011, **65**, 4, 591-594.
77. W. Hu, Y. Chen, H. Yuan, G. Li, Y. Qiao, Y. Qin and S. Feng, *The Journal of Physical Chemistry C*, 2011, **115**, 18, 8869-8875.
78. S. Kumar Srivastav, N. S. Gajbhiye and A. Banerjee, *Journal of Applied Physics*, 2013, **113**, 20, 203917.
79. D. Kothari, V. R. Reddy, A. G. V. Sathe, A. Banerjee, S. M. Gupta and A. M. Awasthi, *Applied Physics Letters*, 2007, **91**, 20, 202505.
80. T. Caronna, F. Fontana, I. Natali Sora and R. Pelosato, *Materials Chemistry and Physics*, 2009, **116**, 2-3, 645-648.
81. A. Z. Simoes, F. G. Garcia and C. D. Riccardi, *Materials Chemistry and Physics*, 2009, **116**, 2-3, 305-309.
82. T. T. Carvalho, J. R. A. Fernandes, J. Perez de la Cruz, J. V. Vidal, N. A. Sobolev, F. Figueiras, S. Das, V. S. Amaral, A. Almeida, J. Agostinho Moreira and P. B. Tavares, *Journal of Alloys and Compounds*, 2013, **554**, 97-103.
83. J. R. Chen, W. L. Wang, J. B. Lia and G. H. Rao, *Journal of Alloys and Compounds*, 2008, **459**, 1-2, 66-70.
84. P. Pandit, S. Satapathy, P. Sharma, P. K. Gupta, S. M. Yusuf and V. G. Sathe, *Bulletin of Materials Science*, 2011, **34**, 4, 899-905.
85. P. Ren, N. Masó, Y. Liu, L. Ma, H. Fan and A. R. West, *Journal of Materials Chemistry C*, 2013, **1**, 13, 2426-2432.
86. L. Gil-Escrig, M. Prades, H. Beltran, E. Cordoncillo, N. Maso, A. R. West, *Journal of the American Ceramic Society*, 2014, in press, DOI: 10.1111/jace.34147.
87. D. Damjanovic, in *The Science of Hysteresis*, eds. G. Bertotti and I. D. Mayergoyz, Academic Press, Oxford, 2006, pp. 337-465.
88. H. Amorin, C. Correas, P. Ramos, T. Hungria, A. Castro and M. Alguero, *Applied Physics Letters*, 2012, **101**, 17, 172908.

89. Y.-H. Lin, Q. Jiang, Y. Wang, C.-W. Nan, L. Chen and J. Yu, *Applied Physics Letters*, 2007, **90**, 17, 172507.
90. V. Annapu Reddy, N. P. Pathak and R. Nath, *Journal of Alloys and Compounds*, 2012, **543**, 206-212.
91. S. Goswami, D. Bhattacharya and P. Choudhury, *Journal of Applied Physics*, 2011, **109**, 7, 07D737.
92. S. M. Selbach, T. Tybell, M. A. Einarsrud and T. Grande, *Chemistry of Materials*, 2007, **19**, 26, 6478-6484.
93. L. H. Yin, J. Yang, B. C. Zhao, Y. Liu, S. G. Tan, X. W. Tang, J. M. Dai, W. H. Song and Y. P. Sun, *Journal of Applied Physics*, 2013, **113**, 21, 214104.